Geophysical Research Letters

RESEARCH LETTER
10.1029/2019GL083667

A Thermodynamic Pathway Leading to Rapid Intensification of Tropical Cyclones in Shear

Xiaomin Chen[1], **Jun A. Zhang**[1,2], **and Frank D. Marks**[1]

[1]NOAA/AOML Hurricane Research Division, Miami, FL, USA, [2]Cooperative Institute for Marine and Atmospheric Studies, University of Miami, Miami, FL, USA

Key Points:
- The nearly saturated lower-middle troposphere in the inner core region precedes the tropical cyclone (TC) rapid intensification in shear
- The moistening of the inner core region is achieved by a competition between surface heat fluxes, radiation, and ventilation effects
- Vortex alignment benefits the moistening of the TC inner core by reducing ventilation effect

Supporting Information:
- Supporting Information S1

Correspondence to:
X. Chen,
xiaomin.chen@noaa.gov

Citation:
Chen, X., Zhang, J. A., & Marks, F. D. (2019). A thermodynamic pathway leading to rapid intensification of tropical cyclones in shear. *Geophysical Research Letters*, *46*, 9241–9251. https://doi.org/10.1029/2019GL083667

Received 10 MAY 2019
Accepted 25 JUL 2019
Accepted article online 30 JUL 2019
Published online 9 AUG 2019

Abstract Understanding physical processes leading to rapid intensification (RI) of tropical cyclones (TCs) under environmental vertical wind shear is key to improving TC intensity forecasts. This study analyzes the thermodynamic processes that help saturate the TC inner core before RI onset using a column-integrated moist static energy (MSE) framework. Results indicate that the nearly saturated inner core in the lower-middle troposphere is achieved by an increase in the column-integrated MSE, as column water vapor accumulates while the mean column temperature cools. The sign of the column-integrated MSE tendency depends on the competition between surface enthalpy fluxes, radiation, and vertical wind shear-induced ventilation effect. The reduction of ventilation above the boundary layer due to vertical alignment is crucial to accumulate the energy within the inner core region. A comparison of the RI simulation with a null simulation further highlights the impact of vortex structure on the thermodynamic state adjustment and TC intensification.

Plain Language Summary A dry environment is unfavorable for tropical cyclones' development and intensification. Enhanced evaporative cooling from convective downdrafts in the dry environment reduces the temperature and humidity in the low-level region of tropical cyclones, which in turn reduces the number and strength of the buoyant convective updrafts in the inner core of the storm. Under environmental vertical wind shear (i.e., wind speed and/or direction varying with height), the core of a tropical cyclone is tilted, allowing dry air intrusion into tropical cyclone circulation at lower levels. Understanding how the tropical cyclones can overcome the negative impacts of downdraft cooling is crucial to improve the intensity forecast using numerical weather prediction models, particularly the timing of rapid intensification onset. This study presents a potentially important thermodynamic pathway leading to the formation of a nearly saturated inner core of a tropical cyclone preceding rapid intensification, which is in connection with vertical alignment of the storm center at different vertical levels.

1. Introduction

Rapid intensification (RI) forecast of tropical cyclones (TCs) under moderate environmental vertical wind shear (VWS) remains a challenge for the forecasting community (Bhatia & Nolan, 2013). One of the error sources comes from the uncertainties in RI onset timing (e.g., Chen, Xue, & Fang, 2018; Judt & Chen, 2016; Munsell et al., 2017). This uncertainty exacerbates the threat to the population and property in the coastal areas, particularly when RI occurs prior to TC landfall (e.g., Hurricane Harvey [2017] and Michael [2018]). Understanding the key physical processes leading to TC RI is critical for improving the prediction of RI and minimizing the potential damage and loss of life.

Earlier theoretical work found that TCs in a normal tropical maritime environment characterized by a moist-neutral state tend to weaken, as an unsaturated lower-middle troposphere promotes strong convective downdrafts that cool and dry the boundary layer (Emanuel, 1989; Rotunno & Emanuel, 1987). This suggests that the development of a TC requires a favorable thermodynamic state (i.e., more humid) that differs from the typical tropical environment.

Precipitation mode can help us gain insight into the background environment. For example, stratiform precipitation is preferred in an environment with high saturation fraction, as suggested by López Carrillo and Raymond (2005). In recent years, statistical analyses of satellite data sets noted significant increase in the azimuthal coverage of stratiform precipitation in the TC inner core region in all shear-relative quadrants, particularly upshear left, prior to RI onset (e.g., Jiang et al., 2018; Tao et al., 2017). A similar phenomenon is

also mentioned in the numerical simulations of Typhoon Mujigae (2015) under different sea surface temperatures (Chen, Xue, & Fang, 2018): They found that TCs starting RI earlier have much higher stratiform precipitation symmetry in the inner core region than late-RI TCs. The increased symmetry of stratiform precipitation in the inner core region suggests that the free troposphere in the TC core is sufficiently humid prior to RI onset. Consistently, results in idealized simulations (e.g., Kilroy et al., 2017; Nguyen et al., 2008; Rappin & Nolan, 2012) also point toward a nearly saturated TC inner core as a prerequisite for TC intensification.

Complicating this interpretation is the presence of VWS, which tilts the TC vortex and induces mesoscale subsidence, drying the column above the surface circulation (e.g., Jones, 1995; Reasor et al., 2004). Additionally, dry air advected into the TC inner core, either at upper (Frank & Ritchie, 2001), middle (Simpson et al., 1958; Tang & Emanuel, 2010), or low levels (Gu et al., 2015; Riemer et al., 2010; Zhang et al., 2013) can ventilate the TC by diluting the warm core, reducing the buoyancy of updrafts, or inducing downdrafts into the boundary layer. The thermodynamic or dynamic processes that resist the ventilation and contribute to the formation of a nearly saturated core in the sheared environment remain to be thoroughly examined.

This study investigates these processes through analysis of the triple-nested (18/6/2 km), cloud-permitting simulation datasets of Typhoon Vicente (2012) with the Weather Research Forecast model (CTL experiment; see details in Chen et al., 2017). Chen, Wang, et al. (2018) revealed that Typhoon Vicente underwent downshear reformation under moderate VWS (8–10 m/s), a rarely documented, but effective dynamic pathway for realignment of the vortex and may lead to TC intensification (see also in Molinari et al., 2006). The interaction between surface enthalpy fluxes and the TC circulation is found to play a prominent role in strengthening and vertically aligning of the reformed inner vortex. However, the associated/accompanying thermodynamic processes that trigger RI are yet to be analyzed or understood clearly. Toward this end, this study focuses on the adjustment of the thermodynamic state of the inner core environment prior to RI onset and investigates various thermodynamic processes (including surface enthalpy fluxes) that modulate this adjustment in a framework of column-integrated moist static energy (MSE). Our aim is to understand the thermodynamic pathway leading to RI onset, clarifying a potentially important RI onset mechanism in shear.

2. Methods

MSE is a useful thermodynamic variable for studying convective process due to its approximate conservation under adiabatic motions (i.e., unchanged column integral). Column-integrated MSE budget is widely used to study various tropical systems, including tropical convergence zone (e.g., Needlin & Held 1987), Madden-Julian oscillation (e.g., Sobel et al., 2014), and TCs (e.g., Frank 1977; Emanuel 2018). This study adopts the column-integrated MSE budget to evaluate the various thermodynamic processes that govern the adjustment of the thermodynamic state in the TC core region. The goal is to understand how the nearly saturated inner core is achieved before RI onset. The budget equation is (Sobel et al., 2014)

$$\left\langle \frac{\partial \left(c_p T + L_v q\right)}{\partial t} \right\rangle = -\left\langle \boldsymbol{u}\cdot\nabla\left(c_p T + L_v q\right)\right\rangle - \left\langle \omega \frac{\partial h}{\partial p} \right\rangle + SFX + \left\langle c_p \left(\frac{\partial \theta}{\partial t}\right)_R \right\rangle, \tag{1}$$

where h denotes MSE ($h = c_pT+gz+L_vq$), T is the temperature, q is specific humidity, c_p is the dry air heat capacity at constant pressure (1,004 $J\cdot K^{-1}\cdot kg^{-1}$), L_v is the latent heat of condensation (treated as constant at 2.5×10^6 J/kg), $\boldsymbol{u}$ is the horizontal velocity, and ω is the vertical velocity. The angle bracket denotes the mass-weighted vertical integration from surface to 100 hPa. *SFX* denotes the surface enthalpy fluxes including latent and sensible heat fluxes. $\left(\frac{\partial\theta}{\partial t}\right)_R$ represents radiative heating/cooling from longwave and shortwave radiation. Here c_pT+L_vq instead of h is used in the time derivative and horizontal advection terms, as we found this form of equation (1) leading to a better closure of the MSE budget, which is consistent with Neelin (2007). The first two terms on the right-hand side (*rhs* hereafter) of equation (1) are horizontal advection of enthalpy and vertical advection of MSE (i.e., HADV and VADV), respectively. The third and fourth terms are source terms.

The TC center at a given pressure level is defined as the geopotential height centroid following Chen, Wang, et al. (2018). This method of identifying the TC center is best when the circulation is weak and loosely

organized (e.g., Nguyen et al., 2014). Vortex tilt is calculated as the distance between the centers at different pressure levels.

3. Results

The simulated Typhoon Vicente (2012) initiates its RI when the 200- to 850-hPa VWS is 8–10 m/s (Figure 1a). The VWS is calculated within 300- to 800-km radii of the surface TC center. The increase in maximum 10-m wind speed (VMAX) during RI (i.e., 0200 UTC 23 July to 1900 UTC 23 July) is greater than 20 m/s, exceeding the RI criteria for TCs in the South China Sea (i.e., VMAX increases by 15 m/s within a day, Chen et al., 2015). The simulated Vicente undergoes substantial structural change prior to RI onset (i.e., $t = -14$–0 hr relative to RI onset). The number of convective bursts (CBs) in the inner core region steadily increases and reaches its peak at 1800 UTC 22 July (i.e., $t = -8$ hr, Figure 1b). One hour later, the reformed inner vortex becomes dominant in the inner core region (see Figure S2 in the supporting information). As in Chen, Wang, et al. (2018), a CB is defined when the maximum vertical velocity at a grid point in the column is greater than 3 m/s. The 300- to 900-hPa vortex tilt reduces with time due to downshear reformation, accompanied by a substantial contraction of the radius of maximum wind (Figure 1b).

Figure 1c shows the evolution of the mean thermodynamic state in the inner core region, measured by the column-integrated MSE, prior to and after RI onset. The area for averaging is selected as a 300 × 300-km box around of the surface TC center. The size of the box is chosen to encompass the inner core region (i.e., radius of maximum wind scale) prior to RI onset (see Figure 1b). The mean column-integrated MSE declines with time until $t = -5$ hr relative to RI onset, followed by a steady increase through the early RI period. This suggests that the increase in the column-integrated MSE is potentially an important thermodynamic precursor to RI. The mean precipitable water (vapor) evolves with time in a similar manner as the column-integrated MSE: It decreases during t = -10 to -5 hr, followed by a subsequent increase. This suggests that the variations in the column-integrated MSE are closely related to that in the latent heat energy (L_vq, see equation (1)) in this column, consistent with the findings of Sobel et al. (2014) and Wing et al. (2016). Note that the column-integrated MSE after $t = -5$ hr is lower than that during $t = -14$ to -8 hr. This is mainly attributed to the opposite tendency of internal energy (c_pT) after $t = -5$ hr to the tendency of L_vq after $t = -5$ hr (Figure 1d), and the steady decrease in c_pT partially counteracts the increase in L_vq. The variation in column-integrated potential energy (gz) is small either prior to RI or through the RI period, suggesting that the steady state presumption for the equation (1) is approximately satisfied within the 300 × 300-km box.

Figure 2 shows the mean MSE and saturated MSE profiles averaged in the same box during $t = -14$ to -12 hr relative to the RI onset (referred to as period 1), $t = -6$ to -4 hr (referred to as period 2), and $t = -2$–0 hr (referred to as period 3). While the column-integrated MSE decreases from period 1 to period 2 (i.e., first stage), the variation in the vertical structure of MSE with time is complex. Both the saturated and unsaturated MSE decreases with time below 400 hPa, while they both increase above 400 hPa. While the relative humidity (RH) below 700 hPa remains the same, it increases by 5–10% within the 700- to 250-hPa layer. This increase in RH is in part due to the increase in specific humidity (Figure 2c). The cooling in the 400–700 hPa also plays a role (Figure 1d, see also the decrease in the saturated MSE). The variations in temperature, specific humidity, and the MSE profile suggest enhanced convective mixing within the column during this period, which is consistent with increase in CB number as shown in Figure 1b.

The evolution of the MSE profile from period 2 to period 3 (i.e., second stage) indicates that the MSE generally increases above ~800 hPa, leading to a net amplification of the column-integrated MSE during this stage (Figure 1c). The whole column is humidified more prominently during this stage: The RH above 900 hPa increases by ~15% and, importantly, the lower-middle troposphere in the inner core region becomes nearly saturated with the RH reaching a mean value of ~90% right before the RI onset. As in the first stage, the increase in RH is attributed to the accumulation of water vapor above 800 hPa (Figure 2c) and the cooling below 400 hPa (Figure 2d). The cooling is mainly attributed to convective mixing and the reduction of subsidence warming as vortex aligns.

Figures 1 and 2 overall suggest that a nearly saturated TC inner core in the lower-middle troposphere is achieved via two stages of moistening, and the moistening is much more effective in the second stage

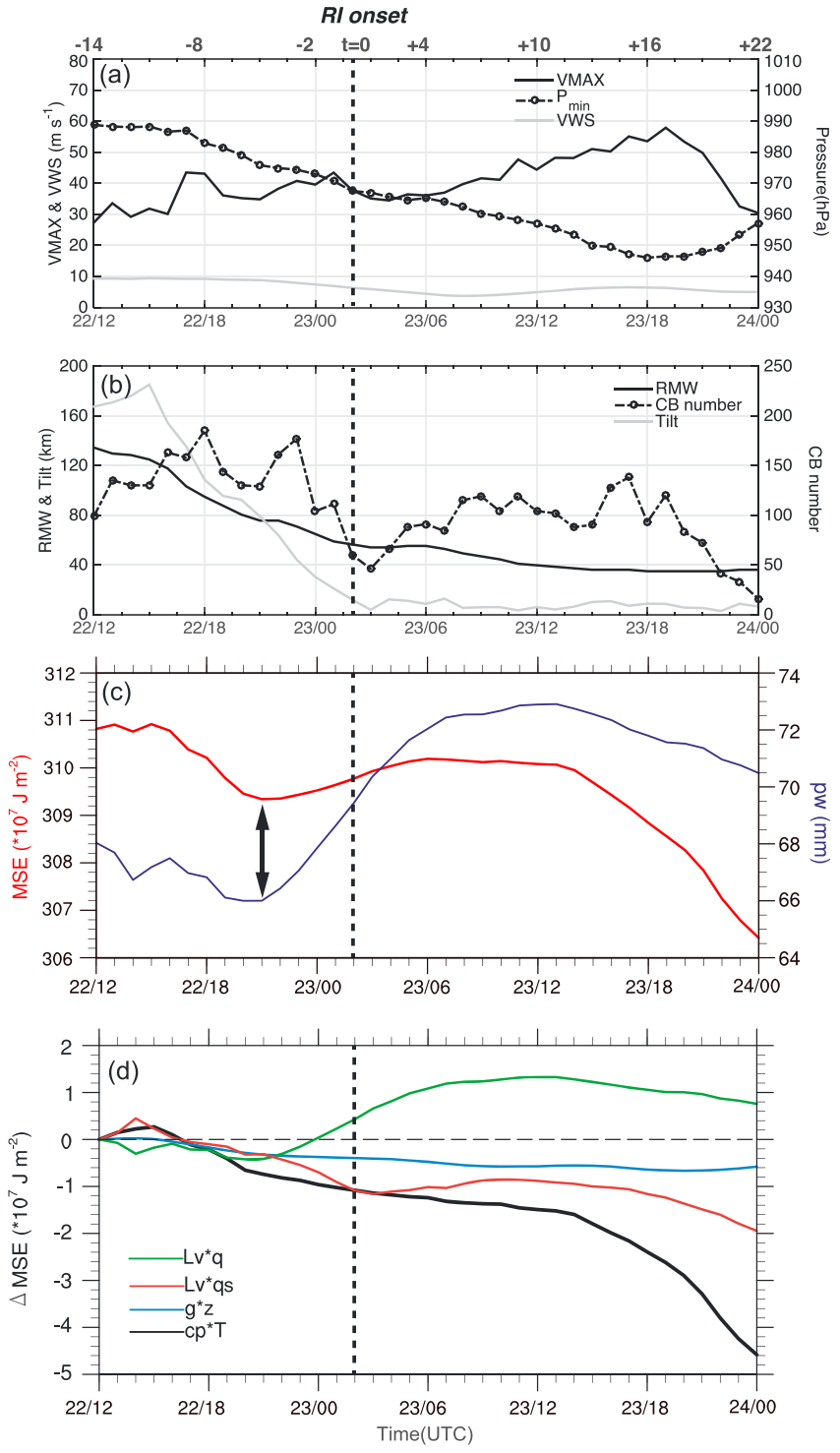

Figure 1. (a) Evolution of the simulated minimum sea level pressure (dashed black with circle, hPa), maximum 10-m wind speed (solid black, m/s), and the magnitude of 200- to 850-hPa vertical wind shear (gray, m/s) from 1200 UTC 22 July to 0000 UTC 24 July. (b) As in (a) but for radius of maximum wind at 10-m height (km) and 300-900 hPa vortex tilt magnitude (km), and number of CBs within a 300 × 300-km box centered on the surface TC center. (c) Column-integrated moist static energy ($\times 10^7$ J/m^2) and precipitable water (mm) averaged within the same box for convective burst number. (d) Evolution of the differences in c_pT (black), gz (blue), L_vq (green), and L_vq_s (red; q_s: saturated mixing ratio) relative to their initial state at 1200 UTC 22 July. The vertical dashed line denotes the time of RI onset (i.e., t = 0 hr) and the RI-onset-relative time is shown on the top axis of (a). The thick black arrow in (c) denotes the timing when MSE and precipitable water start to steadily increase. CB = convective burst; MSE = moist static energy; RI = rapid intensification.

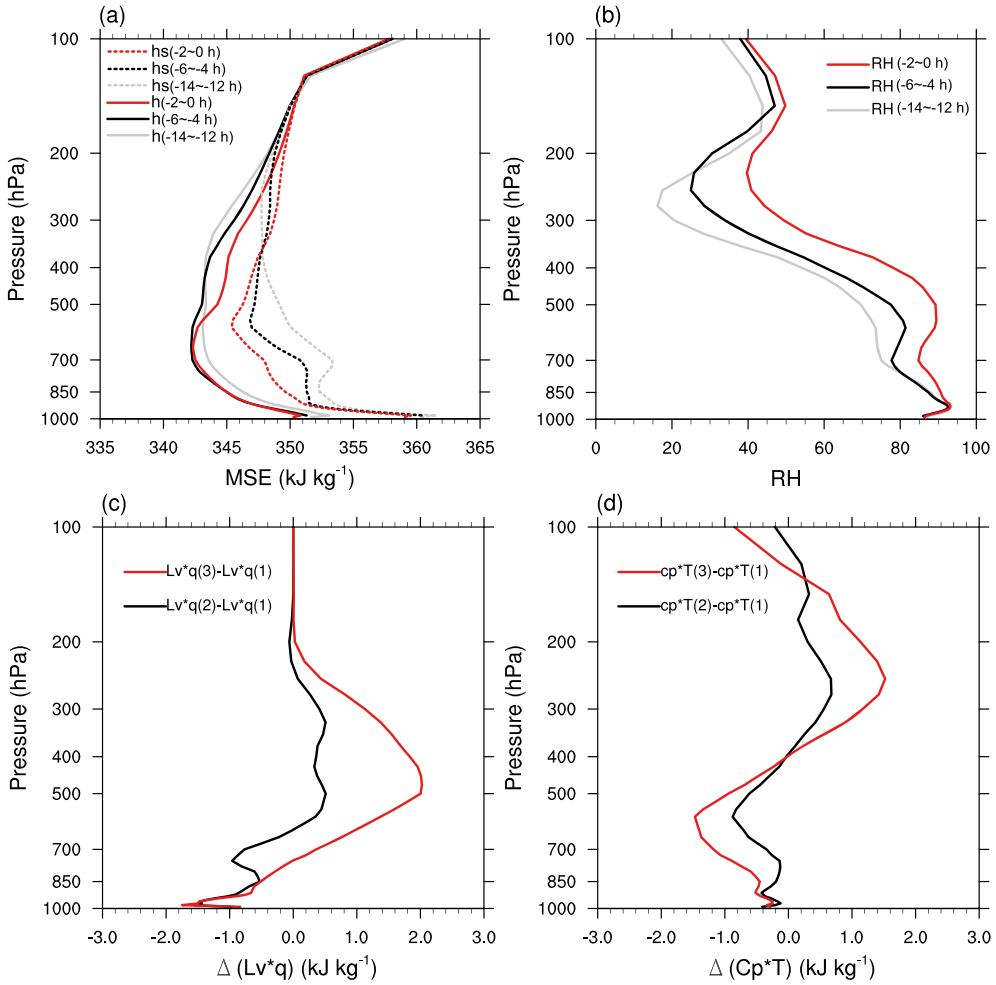

Figure 2. Mean vertical profile of (a) MSE (*h*, solid, kJ/kg) and saturated MSE (*hs*, dashed, kJ/kg), and (b) RH (%) averaged within the 300 × 300-km box centered at the surface tropical cyclone center during 1200–1400 UTC 22 July (period 1, gray), 2000–2200 UTC 22 July (period 2, black), and 0000–0200 UTC 23 July (period 3, red). Variations in the vertical profile of (c) latent heat (kJ/kg), and (d) internal energy (kJ/kg) from period 1 to (black) period 2 and (red) period 3. MSE = moist static energy; RH = relative humidity.

when the column-integrated MSE steadily amplifies. The more notable increase in specific humidity during the second stage (Figure 2c) is seemingly inconsistent with halved CBs number compared to that during the first stage (Figure 1b). We demonstrate later that the differences in moistening and column-integrated MSE tendency between the two stages are also impacted by the variations in inner core structure.

Figure 3 shows the time series of column-integrated MSE budget terms from 1200 UTC 22 July to 1800 UTC 23 July. For simplicity, the budget terms are not shown following landfall. To be consistent with the evolution of the MSE vertical profile, each budget term is averaged in the same box as in Figure 2. Particular attention is paid to the period prior to RI onset (i.e., $t = -$ 14-0 hr). Budget results indicate that the true column-integrated MSE tendency (*lhs* of equation (1)) is generally consistent with the sum of the budget terms on the *rhs* of equation (1). Note that equation (1) neglects the kinetic energy generation term, which may partially account for the residual between *lhs* and *rhs* of equation (1). The budget calculation using the 10-min model output is another potential contributor to this residual, especially when the TC tilt is large and middle-upper tropospheric winds crossing the boundary of budget box are strong (see later discussion).

Surface enthalpy fluxes contribute positively to the increase in the column-integrated MSE, with their magnitude amplifying with time (Figure 3a). In contrast, the column-integrated radiative heating term is

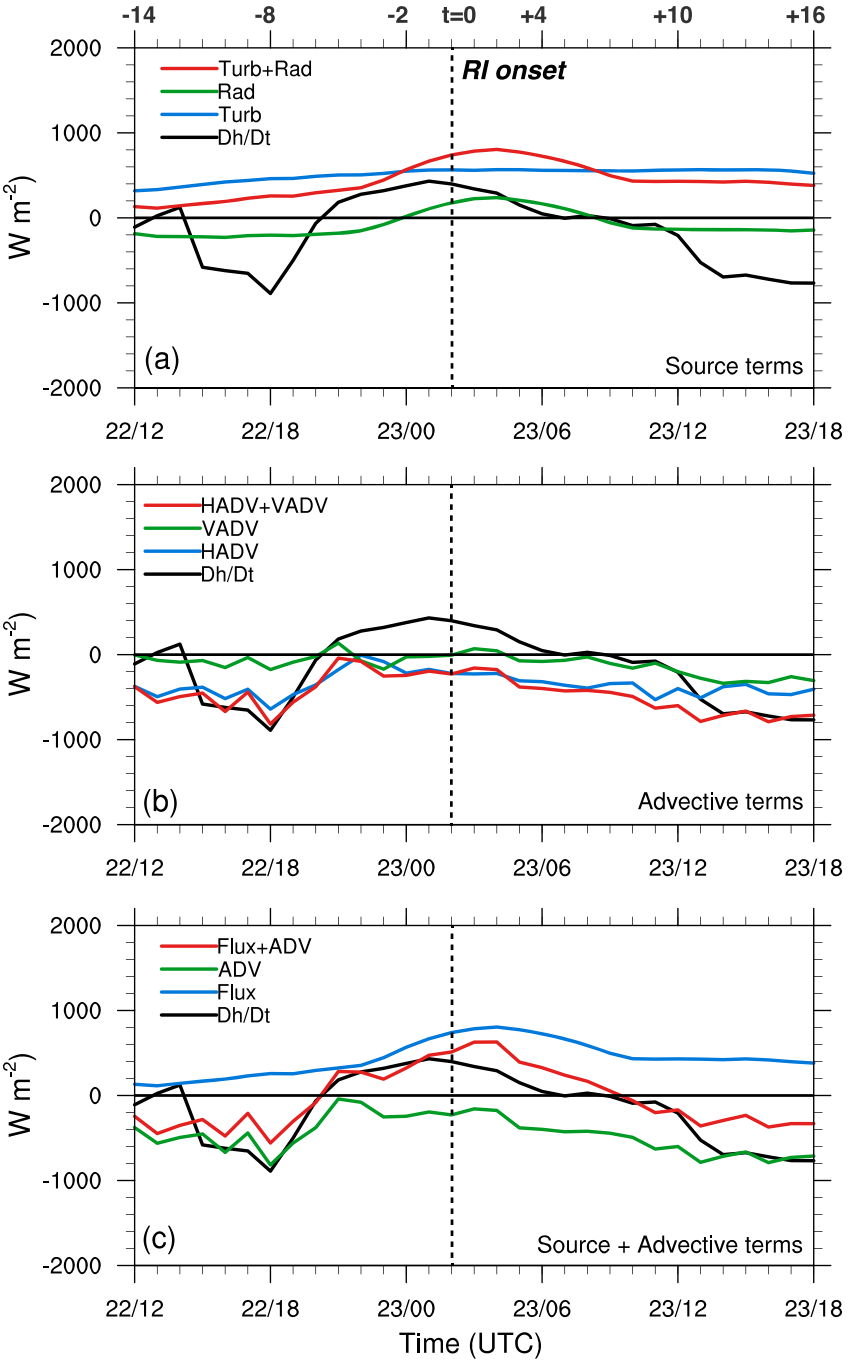

Figure 3. Column-integrated moist static energy budget terms averaged within the 300 × 300-km box centered of the surface tropical cyclone center. (a) Source terms: surface enthalpy fluxes (blue), column-integrated radiative flux (green), and their sum (red); (b) advective terms: HADV, VADV, and their sum; (c) sum of source (blue) and advective terms (green) and their sum (red). The black line in each panel denotes the time derivative of moist static energy. The units are watts per square meter. The RI-onset-relative time is shown on the top of (a). HADV = horizontal advection of enthalpy; RI = rapid intensification; VADV = vertical advection of enthalpy.

negative at nighttime (i.e., $t = -14$ to -4 hr), which is due to the longwave radiative cooling (Figures 4a and 4b). Notably, the radiative cooling below 250 hPa diminishes as the cloud coverage increases significantly (Figure 4d). After sunrise (i.e., approximately $t = -4$ hr), the solar shortwave radiation effectively warms the troposphere, particularly above 600 hPa (Figure 4c), and the column-integrated net radiative heating becomes positive after $t = -2$ hr (Figure 3a).

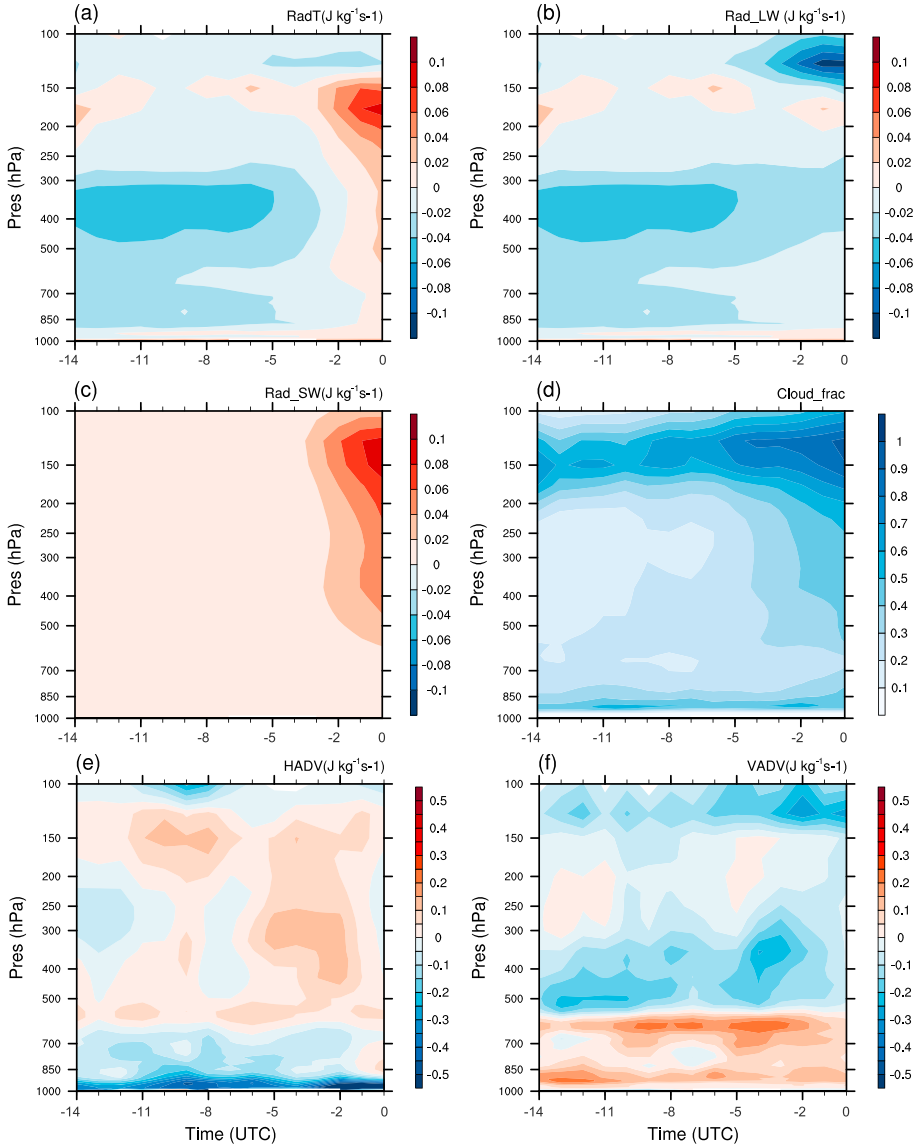

Figure 4. Time series of moist static energy budget terms and cloud fraction prior to rapid intensification onset ($t = -14$–0 hr). Areal-averaged (a) total radiative forcing, (b) longwave and (c) short radiative forcing, (d) cloud fraction (%), and (e) horizontal and (f) vertical advection of moist static energy. The unit for budget terms is Joules per kilogram per second.

Figure 3b shows that the column-integrated advective terms are generally negative both prior to RI onset and throughout the RI period. The VADV term is negligible prior to RI onset because the positive contribution below ~600 hPa is compensated by the negative contribution above (Figure 4f). This structure of VADV is largely accounted for by the vertical advection of mean MSE, which has a local minimum near 600 hPa (Figure 2a), by the mean ascending motion (not shown). The sum of the advective terms in this case can then be approximated by the HADV term. The evolution of HADV is approximately in phase with the tendency of the column-integrated MSE (Figure 3b), as the reduction in MSE during stage 1 and the subsequent increase in stage 2 are primarily attributed to variations in the HADV term. The budget volume cannot accumulate energy from the source terms until HADV is >-400 W/m^2 at $t = -6$ hr (Figures 3b and 3c), highlighting the important role of the HADV term in determining the tendency of the column-integrated MSE.

To understand the processes leading to variations in the HADV term, Figure 4e shows the evolution of its vertical structure prior to RI onset. The negative column-integrated HADV arises mainly from strongly

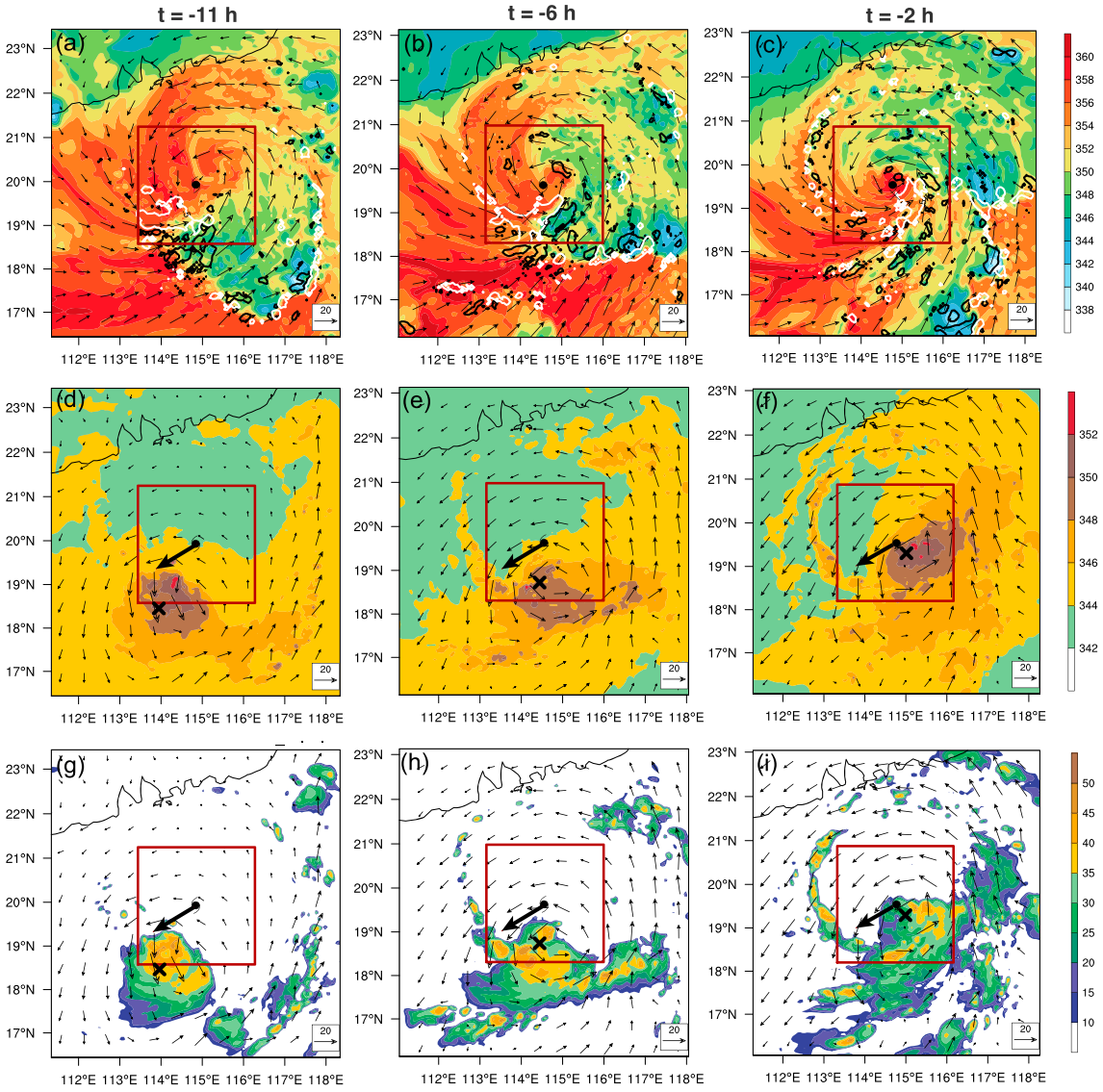

Figure 5. (a–c) Plan view of moist static energy/c_p at the lowest model level (shading, kJ/kg), downward motion at 1-km height (black contour, −0.2 m/s), upward motion at 2-km height (white contour, 0.5 m^{-1}), and storm-relative 10-m winds (vector, m/s) at $t = -11$ hr, $t = -6$ hr, and $t = -2$ hr. (d–f) As in (a–c) but for 300-hPa moist static energy/c_p and storm-relative winds. (g–i) As in (d–f) but for 300-hPa radar reflectivity (shading, dBz) and storm-relative winds. The red square is the 300 × 300 budget box. The vector in each panel represents the 200- to 850-hPa vertical wind shear. The black hurricane and cross symbols denote the surface tropical cyclone center and the 300-hPa tropical cyclone center, respectively.

negative contributions from lower levels (<700 hPa), as the inflow in the lower troposphere advects the low-MSE air parcels downstream of regions of organized convective rainband (denoted as updraft region at 2-km height in Figures 5a–5c) toward the inner core. The low-MSE air parcels at the lowest model level are mostly collocated with the downdraft at 1-km height (e.g., Figures 5a and 5b), suggesting that the low-MSE air parcels originate from the layer above the boundary layer. This low-level ventilation pathway is consistent with that proposed by Riemer et al. (2010). Variations in the magnitude of the HADV term at lower levels are closely connected to the convective activity. The increasing number of CBs during $t = -14$ to −8 hr (Figure 1b) leads to stronger low-level ventilation and thereby more negative HADV in that layer. Similarly, the reduction of the negative HADV at lower levels during $t = -8$ to −4 hr is due to a temporary decrease in convective activity. This decrease is responsible in part for the reduction in magnitude of the negative column-integrated HADV during this period. The development of persistently positive HADV above 700 hPa, with a maximum within the 300- to 250-hPa layer, also contributes to this

reduction of the negative column-integrated HADV before RI onset. The following analysis will demonstrate how this transition is achieved via vertical alignment of the tilted TC vortex.

Figures 5d–5i clearly show that the upper-level vortex gradually intensifies with time, precesses from the downshear left to upshear flank, and undergoes vertical alignment. The convective updrafts transport high-MSE parcels in the boundary layer upward, inferred from the overlapped convective region and high-MSE area. At $t = -11$ hr, the high-MSE region, residing near the left-bottom corner of the budget area due to large vortex tilt, is advected outward by the storm-relative northerly winds at 300 hPa (Figure 5d; termed as upper-level ventilation), leading to negative HADV at this level. As the upper-level vortex moves into the upshear flank after $t = -2$ hr and realigns with the lower-level vortex, the more organized TC circulation and northeasterly upper-tropospheric mean winds advect the high-MSE parcels into the box and the lower-MSE ones out of the box, causing a net increase in the HADV term. In this way, vertical alignment plays an important role in storing the energy within the column of the inner core region. Meanwhile, as the vortex vertically aligns, the tilt-related precipitation rainband moves closer to the TC center (e.g., Figures 5g–5i) and the areal cloud coverage within the inner core region increases (Figure 4d). This increase in cloud coverage reduces the outgoing longwave radiation from the column, another contributor to the increase of column-integrated MSE.

The MSE budget results can help elucidate the moistening process in the lower-middle troposphere. During the first stage, when vortex tilt is relatively large, a warm and dry layer induced by mesoscale subsidence caps over the lower-level circulation of the reformed inner vortex (Figure S3a), consistent with the observational results in Zawislak et al. (2016) and Nguyen et al. (2017). Mesoscale subsidence weakens over the low-level vortex as the vortex tilt reduces and so does the related drying and warming effect (Figure S3b). Meanwhile, the tilt-related convective rainband becomes located closer to the center during the vertical alignment. While the MSE decreases below 400 hPa, the increasing convective mixing cools and moistens the 400- to 700-hPa layer. The lower troposphere (<700 hPa) is one exception, as RH maintains its value during this stage. The moistening effect of convective mixing (or vertical advection) is partially countered by low-level ventilation, leading to net drying and cooling in this layer. During the second stage, the more notable vertical alignment and more humid lower-middle levels reduce the ventilation effect in the 900- to 700-hPa layer. The increase in the column-integrated MSE benefits the formation of a nearly saturated inner core in the lower-middle troposphere at RI onset.

4. Discussion and Conclusions

This study examines the adjustment of the thermodynamic state prior to the RI onset of Typhoon Vicente (2012). We found that most of the free troposphere in the vortex core becomes sufficiently humid prior to RI onset. Insight into the mechanisms leading to moistening is presented based on the column-integrated MSE budget.

Results indicate that the nearly saturated lower-middle troposphere within the TC inner core region at RI onset is achieved via a complex competition between surface enthalpy fluxes, cloud-radiation feedbacks, and ventilation effects. The sign of the column-integrated MSE tendency is largely determined by the ventilation effects. Initially, when the vortex tilt is large, the ventilation is strong, and the column-integrated MSE decreases due to water vapor loss and net column cooling. The moistening of the inner core region is slow.

As TC vortex becomes vertically aligned before RI onset, the column-integrated MSE steadily increases as the ventilation effect above the boundary layer weakens. Meanwhile, the increasing surface enthalpy fluxes support more convection in the tilt-related convective rainband (see Figure S4), which is located closer to the surface TC center as TC vortex aligns. Their aggregate effect is to increase the water vapor in the column and further cool the column, leading to a more efficient moistening of the inner core region. The lower-middle troposphere becomes nearly saturated at RI onset.

A comparison with a slow intensification (non-RI) simulation of the same storm (see Text S1) indicates that the increase in the column-integrated MSE in a necessary, but not sufficient, condition for the RI occurrence, as the column-integrated MSE for the non-RI TC also increases before its slow intensification. This finding is in line with the results in Juračić and Raymond (2016), as they found that the column integral of moist entropy increases for intensifying TCs. However, in the RI simulation, the mean column temperature

within the inner core region is cooler (Figures S5d and S6d) and the RH in the 250- to 700-hPa layer is higher before RI onset (Figure S6b). The cooler column in the RI simulation is primarily attributed to the smaller vortex tilt and the resulting weaker subsidence warming and more convective mixing compared to those in the non-RI simulation (Figure S5b).

The merit of this study is relating the thermodynamic processes to dynamical processes (i.e., vertical alignment) before RI onset under moderate vertical wind shear, in a box-average sense. In nature, the vertical alignment and inner core moistening are three-dimensional formulations. Further examination of the inner core moistening and precipitation evolution before RI onset in a shear-relative framework is of priority in the future work.

Acknowledgments

The authors express thanks to NCAR's Data Support Section for providing the ERA-Interim data (https://rda.ucar.edu/datasets/ds627.0/). This research had been supported by the National Key R&D Program of China under Grant 2017YFC1501601; the Natural Science Foundation of China Grants 41875067 and 41605033. The authors acknowledge Profs. Kerry A. Emanuel and Juan Fang for their instructive comments on this research. We want to acknowledge Paul Reasor, Robert Rogers, Sim Aberson, and two anonymous reviewers for their helpful suggestions to improve this manuscript. The first author, Xiaomin Chen, is supported by a NRC Research Associateship award. Jun Zhang is supported by NOAA Grant NA14NWS4680030 and NSF Grant AGS-1822128.

References

Bhatia, K. T., & Nolan, D. S. (2013). Relating the skill of tropical cyclone intensity forecasts to the synoptic environment. *Weather and Forecasting*, *28*(4), 961–980. https://doi.org/10.1175/WAF-D-12-00110.1

Chen, X., Wang, Y., Fang, J., & Xue, M. (2018). A numerical study on rapid intensification of Typhoon Vicente (2012) in the South China Sea. Part II: Roles of inner-core processes. *Journal of the Atmospheric Sciences*, *75*(1), 235–255. https://doi.org/10.1175/JAS-D-17-0129.1

Chen, X., Wang, Y., & Zhao, K. (2015). Synoptic flow patterns and large-scale characteristics associated with rapidly intensifying tropical cyclones in the South China Sea. *Monthly Weather Review*, *143*(1), 64–87. https://doi.org/10.1175/mwr-d-13-00338.1

Chen, X., Wang, Y., Zhao, K., & Wu, D. (2017). A numerical study on rapid intensification of Typhoon Vicente (2012) in the South China Sea. Part I: Verification of simulation, storm-scale evolution, and environmental contribution. *Monthly Weather Review*, *145*(3), 877–898. https://doi.org/10.1175/MWR-D-16-0147.1

Chen, X., Xue, M., & Fang, J. (2018). Rapid intensification of Typhoon Mujigae (2015) under different sea surface temperatures: Structural changes leading to rapid intensification. *Journal of the Atmospheric Sciences*, *75*(12), 4313–4335. https://doi.org/10.1175/JAS-D-18-0017.1

Emanuel, K. (2018). 100 years of progress in tropical cyclone research. *Meteorological Monographs*, *59*, 15.1–15.68. https://doi.org/10.1175/AMSMONOGRAPHS-D-18-0016.1

Emanuel, K. A. (1989). The finite-amplitude nature of tropical cyclogenesis. *Journal of the Atmospheric Sciences*, *46*(22), 3431–3456. https://doi.org/10.1175/1520-0469(1989)046<3431:TFANOT>2.0.CO;2

Frank, W. M. (1977). The structure and energetics of the tropical cyclone II. Dynamics and energetics. *Monthly Weather Review*, *105*(9), 1136–1150. https://doi.org/10.1175/1520-0493(1977)105<1136:TSAEOT>2.0.CO;2

Frank, W. M., & Ritchie, E. A. (2001). Effects of vertical wind shear on the intensity and structure of numerically simulated hurricanes. *Monthly Weather Review*, *129*(9), 2249–2269. https://doi.org/10.1175/1520-0493(2001)129<2249:EOVWSO>2.0.CO;2

Gu, J.-F., Tan, Z.-M., & Qiu, X. (2015). Effects of vertical wind shear on inner-core thermodynamics of an idealized simulated tropical cyclone. *Journal of the Atmospheric Sciences*, *72*(2), 511–530. https://doi.org/10.1175/JAS-D-14-0050.1

Jiang, H., Zagrodnik, J. P., Tao, C., & Zipser, E. J. (2018). Classifying precipitation types in tropical cyclones using the NRL 37 GHz color product. *Journal of Geophysical Research: Atmospheres*, *123*, 5509–5524. https://doi.org/10.1029/2018JD028324

Jones, S. C. (1995). The evolution of vortices in vertical shear. I: Initially barotropic vortices. *Quarterly Journal of the Royal Meteorological Society*, *121*(524), 821–851. https://doi.org/10.1002/qj.49712152406

Judt, F., & Chen, S. S. (2016). Predictability and dynamics of tropical cyclone rapid intensification deduced from high-resolution stochastic ensembles. *Monthly Weather Review*, *144*(11), 4395–4420. https://doi.org/10.1175/MWR-D-15-0413.1

Juračić, A., & Raymond, D. J. (2016). The effects of moist entropy and moisture budgets on tropical cyclone development. *Journal of Geophysical Research: Atmospheres*, *121*, 9458–9473. https://doi.org/10.1002/2016JD025065

Kilroy, G., Smith, R. K., & Montgomery, M. T. (2017). A unified view of tropical cyclogenesis and intensification. *Quarterly Journal of the Royal Meteorological Society*, *143*(702), 450–462. https://doi.org/10.1002/qj.2934

López Carrillo, C., & Raymond, D. J. (2005). Moisture tendency equations in a tropical atmosphere. *Journal of the Atmospheric Sciences*, *62*(5), 1601–1613. https://doi.org/10.1175/JAS3424.1

Molinari, J., Dodge, P., Vollaro, D., Corbosiero, K. L., & Marks, F. (2006). Mesoscale aspects of the downshear reformation of a tropical cyclone. *Journal of the Atmospheric Sciences*, *63*(1), 341–354. https://doi.org/10.1175/JAS3591.1

Munsell, E. B., Zhang, F., Sippel, J. A., Braun, S. A., & Weng, Y. (2017). Dynamics and predictability of the intensification of Hurricane Edouard (2014). *Journal of the Atmospheric Sciences*, *74*(2), 573–595. https://doi.org/10.1175/JAS-D-16-0018.1

Neelin, J. D. (2007). Moist dynamics of tropical convection zones in monsoons, teleconnections and global warming. In T. Schneider, & A. H. Sobel (Eds.), *The global circulation of the atmosphere*, (pp. 267–301). Princeton, NJ: Princeton University Press.

Neelin, J. D., & Held, I. M. (1987). Modeling tropical convergence based on the moist static energy budget. *Monthly Weather Review*, *115*(1), 3–12. https://doi.org/10.1175/1520-0493(1987)115<0003:MTCBOT>2.0.CO;2

Nguyen, L. T., Molinari, J., & Thomas, D. (2014). Evaluation of tropical cyclone center identification methods in numerical models. *Monthly Weather Review*, *142*(11), 4326–4339. https://doi.org/10.1175/MWR-D-14-00044.1

Nguyen, L. T., Rogers, R. F., & Reasor, P. D. (2017). Thermodynamic and kinematic influences on precipitation symmetry in sheared tropical cyclones: Bertha and Cristobal (2014). *Monthly Weather Review*, *145*(11), 4423–4446. https://doi.org/10.1175/MWR-D-17-0073.1

Nguyen, V. S., Smith, R. K., & Montgomery, M. T. (2008). Tropical-cyclone intensification and predictability in three dimensions. *Quarterly Journal of the Royal Meteorological Society*, *134*(632), 563–582.

Rappin, E. D., & Nolan, D. S. (2012). The effect of vertical shear orientation on tropical cyclogenesis. *Quarterly Journal of the Royal Meteorological Society*, *138*(665), 1035–1054. https://doi.org/10.1002/qj.977

Reasor, P. D., Montgomery, M. T., & Grasso, L. D. (2004). A new look at the problem of tropical cyclones in vertical shear flow: Vortex resiliency. *Journal of the Atmospheric Sciences*, *61*(1), 3–22. https://doi.org/10.1175/1520-0469(2004)061<0003:ANLATP>2.0.CO;2

Riemer, M., Montgomery, M. T., & Nicholls, M. E. (2010). A new paradigm for intensity modification of tropical cyclones: Thermodynamic impact of vertical wind shear on the inflow layer. *Atmospheric Chemistry and Physics*, *10*(7), 3163–3188. https://doi.org/10.5194/acp-10-3163-2010

Rotunno, R., & Emanuel, K. A. (1987). An air–sea interaction theory for tropical cyclones. Part II: Evolutionary study using a nonhydrostatic axisymmetric numerical model. *Journal of the Atmospheric Sciences*, *44*(3), 542–561. https://doi.org/10.1175/1520-0469(1987)044<0542:AAITFT>2.0.CO;2

Simpson, R. H., Bureau, U. S. W., & Riehl, H. (1958). Mid-tropospheric ventilation as a constraint on hurricane development and maintenance. Paper presented at the Tech. Conf. on Hurricanes, Miami Beach, FL.

Sobel, A., Wang, S., & Kim, D. (2014). Moist static energy budget of the MJO during DYNAMO. *Journal of the Atmospheric Sciences*, *71*(11), 4276–4291. https://doi.org/10.1175/JAS-D-14-0052.1

Tang, B., & Emanuel, K. (2010). Midlevel ventilation's constraint on tropical cyclone intensity. *Journal of the Atmospheric Sciences*, *67*(6), 1817–1830. https://doi.org/10.1175/2010JAS3318.1

Tao, C., Jiang, H., & Zawislak, J. (2017). The relative importance of stratiform and convective rainfall in rapidly intensifying tropical cyclones. *Monthly Weather Review*, *145*(3), 795–809. https://doi.org/10.1175/MWR-D-16-0316.1

Wing, A. A., Camargo, S. J., & Sobel, A. H. (2016). Role of radiative–convective feedbacks in spontaneous tropical cyclogenesis in idealized numerical simulations. *Journal of the Atmospheric Sciences*, *73*(7), 2633–2642. https://doi.org/10.1175/JAS-D-15-0380.1

Zawislak, J., Jiang, H., Alvey, G. R., Zipser, E. J., Rogers, R. F., Zhang, J. A., & Stevenson, S. N. (2016). Observations of the structure and evolution of Hurricane Edouard (2014) during intensity change. Part I: Relationship between the thermodynamic structure and precipitation. *Monthly Weather Review*, *144*(9), 3333–3354. https://doi.org/10.1175/MWR-D-16-0018.1

Zhang, J. A., Rogers, R. F., Reasor, P. D., Uhlhorn, E. W., & Marks, F. D. (2013). Asymmetric hurricane boundary layer structure from dropsonde composites in relation to the environmental vertical wind shear. *Monthly Weather Review*, *141*(11), 3968–3984. https://doi.org/10.1175/MWR-D-12-00335.1